Heat Input-Driven Microstructural Evolution and Performance Enhancement of TIG-Cladded $AlCoCrFeNiSi_{0.3}$ High Entropy Alloy on Martensitic Stainless Steel

***Rahul Kumar Ravi*[1,2]*, *Jagesvar Verma*[1], *Anoop Kumar Sood*[1]**

[1] *Department of Mechanical Engineering, National Institute of Advanced Manufacturing Technology, Ranchi 834003, India*

[2] *Jharkhand University of Technology, Ranchi 834010, India*

Keywords:

AISI 410 martensitic stainless steel, Tungsten Inert Gas (TIG) Cladding, Microstructure, Solid Solution Strengthening, Potentiodynamic Polarization.

* Corresponding author:

Author (Rahul Kumar Ravi)
E-mail: (Okrahul414@gmail.com)

ABSTRACT

This study investigates the microstructure, mechanical properties, and corrosion behavior of AlCoCrFeNiSi0.3 high entropy alloy cladding deposited on AISI 410 martensitic stainless steel substrate using tungsten inert gas process. The high entropy alloy powder was preplaced as a paste form on the AISI 410 substrate and cladded at three different heat inputs corresponding to current levels - 80A, 100A and 120A (as sample S-80A, S-100A and S-120A) respectively. Higher dilution was measured in high heat input cladded sample. SEM Microstructural analysis revealed columnar and equiaxed grain structures in the cladded zone. X-ray diffraction confirmed the formation of BCC and FCC solid solution phases. Micro-hardness increased with increasing heat input and lowest hardness was obtained in substrate. Potentiodynamic polarization tests in 3.5% NaCl solution indicated improved corrosion resistance of the HEA coatings compared to the bare substrate. The enhanced properties are attributed to solid solution strengthening, lattice distortion, and equiaxed grain formation. The corrosion resistance was increased by formation of a passive film.

1. INTRODUCTION

Martensitic stainless steels (MSSs) are chromium-based SS with a low carbon content has a great demand and used in various components of several industrial sectors such as hydro turbines, turbine blades, automotive components, bearings, cutting tools, cutlery, pump, valve parts, surgical instruments and, under water trolleys [1-6], due to its better corrosion resistance (in mild environment), wear resistance, tensile strength and fatigue strength [2]. Its higher hardness property and better corrosion resistance in less harsh environment makes MSSs suitable for hydro-turbines in hydraulic power plant, offshore and marine industries as a cost-effective SS [1,7]. Among the MSSs, AISI 410 is more popular grade for such plants, however, in harsh environment or the environment where combined effect of wear and corrosion takes place that reduces the life of the materials in spite of its high strength and high hardness properties [3,8]. Several studies show that AISI 410 experiences substantial degradation due to synergy in erosion-corrosion [9-11]. To improve the life of the materials coating/cladding is an effective way, however, nowadays high-entropy alloys (HEAs), known as an emerging class of alloy system, have drawn substantial interest than conventional alloys and are extensively investigated [12,13]. It’s four core effects such as high configuration entropy effect, lattice distortion, sluggish effect, and cocktail effect, offer high hardness, excellent oxidation, corrosion and wear resistance compared with conventional alloys makes HEA as a suitable for extreme operating conditions [14-17]. Typically HEAs forms a single phase solid solution which is thermodynamically stable and exhibit unique microstructure and outstanding properties [18,19]. There are several methods of coating to improve surface properties, such as thermal and

plasma spraying coating, chemical vapour deposition, and physical vapour deposition, gas tungsten arc cladding and laser cladding [20,21]. Now a days laser cladding and tungsten inert gas (TIG) cladding is being used prominently.
TIG Cladding is known for its controlled and enhanced localized heat input, offering high quality welds, decreased internal fluid resistance resulting in enhanced microstructure, mechanical properties, corrosion resistance and toughness compared to traditional heat treatment methods which increase applicability in various critical applications [22,23]. Other advantages of TIG cladding are as cooling rates and less thermal effects, enhance metallurgical bonding compared to other cladding methods [22-24]. It is an economical method for coating cladding and surface treatment which ensure a strong bond between cladding layer with the substrate, resulting enhanced microhardness and wear resistance [21,24,25].

In recent years lots of research is going on in the field of HEAs cladding in which TIG cladding is one of the adopted processes. Qingkai et al. prepared AlCoCrFeNi HEA coating on a low-carbon Q235 steel using TIG cladding with varying heat input (840 J/mm-1008 J/mm) and found that at 180 A based heat input gives better corrosion resistance, while 150 A based heat input shows highest hardness (581 HV) [25]. Yilian et al. prepared FeCrNiCoMnSi0.1 and cladded it on 40Cr alloy using TIG and studied the impact of high-frequency ultrasonic. The author found that the ultrasonic impact process increases microhardness by 41%, which is 807 HV by refinement of grains [26]. Hao et al. investigated the two different studies on effect of silicon (Si) addition using laser-cladded behaviour of AlCoCrFeNiSix HEAs on AISI 304 stainless steel and reported that as the Si content increased, the microhardness reached 8.19 GPa maximum for HEA Si0.5, and density dislocation increased, resulting in friction and wear reduction [27,28]. Deepak et al. investigate tribological behaviour and failure behaviour of equiatomic AlCrCuNiFe HEA two separate study have been done on same alloys using of TIG on substrate 1050 steel at room temperature found that improvement in their properties [29,30]. Girisha et al. studied the mechanical behaviour of AISI 410 using plasma-sprayed TiO_2 coating and found that hardness increased by 60% with less porosity (2-3%) compared with substrates [31]. Ramesh et al. investigated hardness, corrosion and wear performance of AISI 410 using manual metal arc welding (MMAW) and friction surfacing (FS), found that MMAW have higher coefficient of friction (0.75±0.05) and FS exhibit better hardness (440±12 HV) and corrosion resistance among them [32].

From the literature and open sources, the utilization of HEAs for various applications for surface modification to enhance the surface properties is on demand, but research on the AISI 410 cladded by AlCoCrFeNiSi0.3 through economical method (TIG cladding) is limited, however, demand of AISI 410 MSS is huge, but poor performance in various sectors is restricted its application. Its characterization in terms of microstructure, mechanical properties and corrosion resistance is scarce. Study on the cladding of low-cost Fe-based AlCoCrFeNiSi0.3 high entropy alloy on AISI 410 cost effective material through economical process (TIG cladding) is so far limited. In this research work AISI 410 MSS is used as a substrate (base metal), which is prime material for hydraulic turbine blade application and AlCoCrFeNiSi0.3 HEA with Si addition is taken as a cladding material. The low cost TIG process with varying heat input is adapted to perform single layer cladding on substrate. The effect of heat input on cladded materials is analyzed in terms of microstructure, phase analysis, mechanical properties and corrosion resistance.

2. MATERIALS AND METHODS

2.1 Sample preparation

The substrate AISI 410 with dimension of 50 mm × 50 mm × 6 mm is cut using wire EDM and prepared for cladding process. The chemical composition of the substrate AISI 410 is given in Table 1. To remove contaminants and oxide layers, the surface has been polished with 240 and 300 grit emery paper and then washed with acetone. The coating material consists of a high entropy alloy designated as AlCoCrFeNiSi0.3. The composition is presented in Table 2, for the preparation of sample a total of 35 g of powder is taken and each elemental powder (in g) is mentioned in Table 2. The powder has a particle size ranging from 40 to 90 μm and a purity of 99.96%. To mix powder uniformly, a planetary ball milling (Retch PM 400) containing tungsten carbide ball (10:1 ball to powder weight ratio) is used rotating at 350 rpm for 1 hour, the milled powder was mixed with an appropriate 4 wt.% of PVA to prepare the preplaced HEA paste on specimens achieving thickness of 1.5 mm. The paste is placed in a furnace for 2 hours at 80oC temperature to remove moisture contains after that it is used for cladding purposes.

Table 1. Chemical composition of substrate AISI 410 (wt%)

C	Ni	Cr	Mn	Si	Fe
0.11	0.41	12.95	0.82	0.78	Bal.

Table 2. Weight composition of $AlCoCrNiSi_{0.3}$ HEA (Total = 35 g)

Element	Weight (g)	Fractional weight (g/mol)	HEA (wt.%)
Al	3.620	26.982	18.868
Co	7.906	58.933	18.868
Cr	6.975	51.996	18.868
Fe	7.492	55.845	18.868
Ni	7.874	58.693	18.868
Si	1.130	8.4258	5.660

2.2 TIG cladding setup

A MasterTIG MLS 2300ACDC heat source was employed for cladding the dried pre-placed mixed paste onto the steel substrate. To ensure uniform scanning speed, the TIG torch was mounted on an XY table. A tungsten electrode with a diameter of 2.4 mm and a tip angle of 10° was used to produce a stable arc. The fusion zone during the cladding process was shielded with argon gas and a flow rate of 12 l/min. cladding parameters are presented in Table 3.

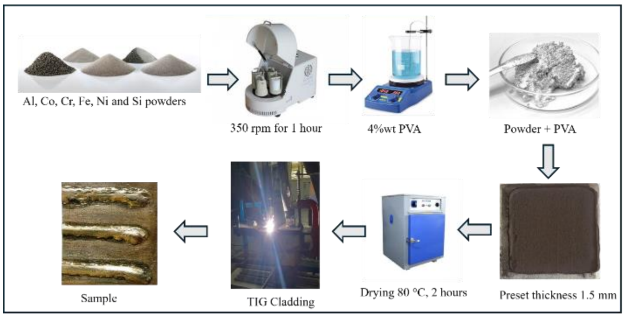

Fig. 1. Schematic diagram of sample preparation procedure

Table 3. TIG parameters

Scanning speed	4 mm/s
Argon flow rate	12 l/min
Tip/torch angle	90^{o}

2.3 Metallography and Characterization

To get the desired dimension of a sample to perform characterizations, wire EDM is used. For metallurgical investigations, samples have been grounded by sandpaper, supplemented by 1μm grit diamond paste and etched by concentrated aqua regia solution (HNO_3: HCL= 1:3) for 4-8 s. The microstructure and phase analysis of the sample is characterized using a FE-SEM equipped with EDAX (Carl Zeiss, Supra 55), and XRD (Rigaku MiniFlex 600) respectively. X-ray diffractometer utilizing Cu-Kα radiation (λ = 1.5406 Å) with diffraction range 30^{o} to 90^{o} and scan speed 2^{o} per minute employed to identify the phases present in the cladded layer, perpendicular to direction of scan. The microhardness is measured by Vickers hardness test (Matsuzawa MMT-X) with dwell time 10 s and load 300 gf is taken, the test is performed as per ASTM E92-17.

Corrosion resistance of substrate and cladded samples is analyzed by potentiodynamic polarization test (Tafel test) succeeded by open circuit potential test (OCP) are performed using an electrochemical workstation (CHI6361E) configured in a three-electrode system, with a 3.5 wt% NaCl solution. The coating sample served as the working electrode, while a graphite electrode and a silver chloride (Ag/AgCl) electrode functioned as the counter and reference electrodes respectively. The open circuit potential was allowed to stabilize for 30 minutes prior to conducting the electrochemical tests. OCP time is 400 s. for each test, -0.3 V vs OCP considered. The corrosion test has been performed over a potential range of -0.12 to +0.06 V relative to the open circuit potential, with a sweep rate of 0.3 mV/s.

3. RESULTS AND DISCUSSION

3.1 Dilution calculation of cladded samples

Samples were prepared by consisting of a high entropy alloy designated as $AlCoCrNiSi_{0.3.}$ The process of preparation is illustrated in Figure 1

The heat input (H.I.) is a critical parameter in TIG cladding and was maintained constantly across all cladding passes. Heat input is calculated using equation [25].

$$H.I. = \frac{\eta\, VI}{\upsilon} \qquad (1)$$

Where, η represents the efficiency of the TIG cladding process, considering 0.7 [25]. Here, I is the welding current (A), V is the voltage, and υ is the travel speed. Average cladding voltage of 12.38-12.71 V is taken for 80A- 120A respectively.

Heat input for the samples S-80A, S-100A and S-120A is 174.41 J/mm, 211.26 J/mm and 247.13 J/mm respectively as mentioned in Table 4. The heat input decided the dilution of the cladding, which further affected the microstructure, mechanical properties, and corrosion resistance of the cladded samples.

Dilution (Φ)is calculated by given equation [33].

$$\Phi = \frac{h}{h+H} \times 100\% \qquad (2)$$

where h means the depth of cladded zone and H means the height of the cladded zone as depicted in Figure 2.

Figure 2 (a) shows the HEA deposited layer and their cross sections with different heat input corresponding to different currents. The total height of the cladding zone, measured from the transition zone, is approximately 1.83 mm, 2.107 mm, and 2.284 mm for the samples processed at 80 A, 100 A, and 120 A, respectively. The corresponding width of the cladded zones are 5.08 mm,6.21 mm, and 6.58 mm for 80 A, 100 A, and 120 A, respectively.

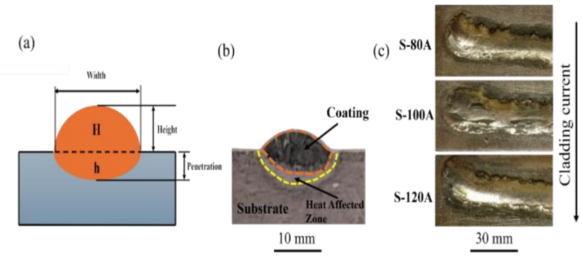

Fig. 2. (a) Schematic representation of dilution, (b) Cross-section of clad, and (c) HEA cladded samples.

High heat input 247.13J/mm associated with high welding speed (4.32 mm/s) showed to a broader width of the cladded zone (6.58mm) and reinforcement (0.67 mm) may be due to higher temperature in the cladded zone. Whereas, low heat input 174.41 J/mm having low cladding speed (3.975 mm/s) directed to 5.08 mm width and 0.34 mm reinforcement owing to lower temperature in the cladded zone, the lower temperature caused increased surface tension and viscosity caused by Marangoni effect led to smaller width resulted in reduction in spreadability due to increasing the surface tension of depth to width ratio of the molten metal [34,35].

Table 4. Heat Input and Dilution calculation

Samples	Current (A)	Travel speed (mm/s)	Heat Input (J/mm)	H (mm)	h (mm)	Dilution (%)
S-80A	80	3.97	174.41	1.490	0.34	18.73
S-100A	100	4.15	211.26	1.619	0.487	23.16
S-120A	120	4.32	247.13	1.607	0.67	29.67

Experimental results demonstrated that the lower cladding current (80 A) having a lower welding heat input led to the development of an improper weld bead shape. Furthermore, the cross-section of the cladded layer produced at a reduced travel speed may affect the dilution of the substrate and cladded layer. However, dilution plays a significant role in solidification cracking and caused to failure if properly not controlled [35]. Dilution is the quantity of the substrate that melts and mixed powder layer constitution. The dilution of S-80A, S-100A and S-120A was 18.73 %, 23.16 % and 29.67 %, respectively, which are near to the optimal dilution as suggested by Fereidouni et al. (25%-35%)[25]

3.2 Thermodynamic calculations of AlCoCrFeNiSi$_{0.3}$

Thermodynamics calculation is also important to predict the structure, which mainly affects the properties, and the composition is also selected based on the desired structure to enhance the mechanical properties such as hardness and wear.

It is known fact that multi principal alloys have very high mixing entropy which helps in prevention of intermetallic formation [36], so, design parameter plays an important role in any HEA design. For solid solution formation some of the parameters are significant such as mixing entropy (ΔS_{mix}), mixing enthalpy (ΔH_{mix}), atomic differences (δ), valence electron concentration (VEC) and parameter omega (Ω) [37]. Role of

Gibbs free energy (ΔG) is more important during prediction of solid solution formation, ΔG in solid solution considered same as ΔG_{mix} at constant temperature. Mathematical relation is as depicted in eq. (3).

$$\Delta G_{mix} = \Delta H_{mix} - T\Delta S_{mix} \qquad (3)$$

Here $T\Delta S_{mix}$ is considered as driving energy and ΔH_{mix} as resistant energy for formation of solid solution. Zhang et al suggested the prediction criteria, if Ω ≥1.1, then it will form a solid solution in HEA, the expressions for HEA is given below as eq. (4-9) [37,38].

$$\Omega = \frac{T_m \Delta S_{mix}}{|\Delta H_{mix}|} \qquad (4)$$

$$T_m = 4\sum_{i=1}^{n} c_i\,(T_m)_i \qquad (5)$$

$$\delta = \sqrt{\sum_{i=1}^{n} c_i\,(1 - \tfrac{r_i}{\bar{r}})^2} \qquad (6)$$

$$\Delta S_{mix} = -R\sum_{i=1}^{n}(c_i Inc_i) \qquad (7)$$

$$\Delta H_{mix} = 4\sum_{i=1}^{n} \Delta H_{ij}^{mix} c_i c_j \qquad (8)$$

$$VEC = \sum_{i=1}^{n} c_i VEC_i \qquad (9)$$

Where T_m is the melting temperature of HEA, C_i is concentration of i^{th} element, r_i is the atomic radius of constituent elements, $\bar{r}$ is the average radius of HEA, R is the universal gas constant (R= 8.314 J/K.mol). The Miedema macroscopic model has been utilized to determine ΔH_{mix}. Nevertheless, specific criteria must be met for the formation of BCC, FCC, and BCC+ FCC structures, encompassing both simple disorder and simple order phases [39]. These criteria are: -10 kJ/mol $<\triangle H_{mix}<$ 5 kJ/mol, $\triangle S_{mix}>$ 13.38 J/K mol and δ < 4% [37]. Additionally, these parameters serve to inhibit intermetallic formation and indicate the conditions for solid solution formation to meet the criteria proposed by researchers [39,40]. H_{mix} should not have a high positive value to prevent phase separation, while a high enthalpy value indicates phase stability, conversely, a highly negative mixing enthalpy results in intermetallic formation [40]. A larger delta (δ) value generates excessive strain energy, disrupting the balance among alloys [37,39]. VEC criteria mainly used to predict the phases, but it may not be accurate, always, for BCC structure prediction, VEC should be ≤ 6.7, while for FCC, it should be VEC ≥ 7.8, when both structures coexist, VEC should fall between these values. 6.7-7.8 for FCC+BCC [40].

Table 5 illustrated the calculated values of $AlCoCrFeNiSi_{0.3}$ alloy based on the empirical relation as mentioned above parameters which indicated that the HEA showed solid solution formation with comprised of BCC and FCC phases.

Table 5. Thermodynamic calculation of $AlCoCrFeNiSi_{0.3}$

Ω	T_m	δ	ΔS_{mix}	ΔH_{mix}	VEC
1.0944	1684.4	6.12	11.816	-18.187	7.0196

3.3 XRD analysis

Figure 3 showed the XRD phase patterns of substrate and $AlCoCrFeNiSi_{0.3}$ HEA cladded layers with varying heat input. XRD analysis showed that All HEA cladded samples have been composed of BCC and FCC phases. The same were also predicted by empirical relation of various parameters [40]. No intermetallics were found, however, it is difficult to detect intermetallic by XRD alone, since the sensitivity of the detector and brilliance of the source are not enough to detect the phases with small volume fractions. All the samples showed many similar peaks, substrate has less peaks compared to cladded layers, near common diffraction peaks at 2θ = 44.56°, 64.96°, and 82.24°. Cladded samples have diffraction at 2θ = 43.53° which is not positioned in substrate.

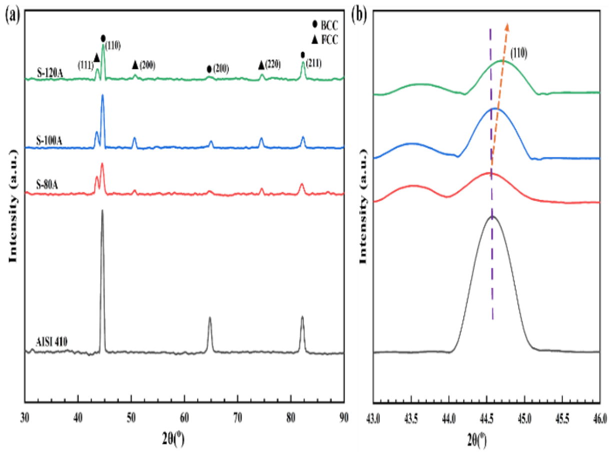

Fig. 3. XRD pattern of (a) substrate and $AlCoCrFeNiSi_{0.3}$, (b) diffraction at 2θ = 44.51°, 44.60°, and 44.69

It is observed that highest diffraction (110) of sample S-80A, S-100A and S-120A have at 44.51°, 44.60°, and 44.69° respectively (Figure 3b), it is also observed that peaks slightly shifted to right with increasing current may be due to residual stress as current increases. This HEA consists of Al and Si as constituent elements, Al has largest, and Si has ssmallest radius, they help in lattice shrinkage to dissolve in solid solution.

3.4 Microstructural Analysis

Figure 4 illustrated microstructure of $AlCoCrFeNiSi_{0.3}$ HEA cladding, the cladding of $AlCoCrFeNiSi_{0.3}$ comprises of HEA cladded zone, transition between cladded zone and substrate mentioned as heat affected zone (HAZ). In general, the heat input corresponding to cladding speed and current plays a very significant role in deciding the microstructure and mechanical properties and corrosion resistance [25,42]. From the micrograph (Figure 4) uniform and dense without crack or pores microstructure were observed for all cladded samples, may be due to the agglomeration and slugging nature of Si and other HEAs [41]. Good metallurgical bonding was believed to be achieved between cladded layers and the substrate. Each sample has two regions in which region “A” has HEA cladding and region “B” has transition zone of cladding.

Low and higher magnification SEM images of cladded zones and substrate microstructure are illustrated in Figure 4(a,b,d,e,g,h) and 4(c,f,i) respectively. The microstructure of all cladded samples is mainly composed of columnar and equiaxed dendritic morphology, whereas substrate is composed of lathy martensite. Figure 4(a,d,g) showed the development of HAZ of respective heat inputs, the formation of HAZ in transition zone was mainly due to high thermal conductivity of AISI 410 MSS caused by thermal gradient resulted in absence of phase change that does not allow the grain refinement [43,44].

From the XRD phase analysis, BCC and FCC phase formation was identified, which was good agreement of empirical relation as mentioned above [40].

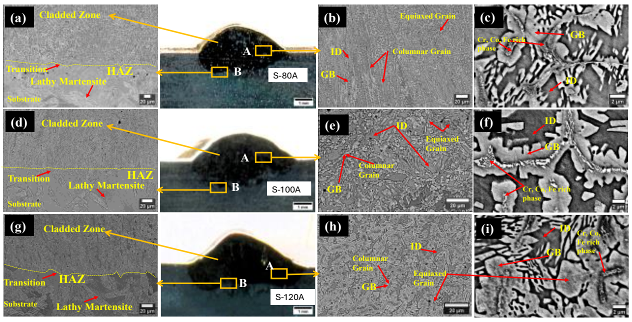

Fig. 4. SEM micrograph of cross section of samples (a)S-80A; (b) S-100A; (c) S-120A

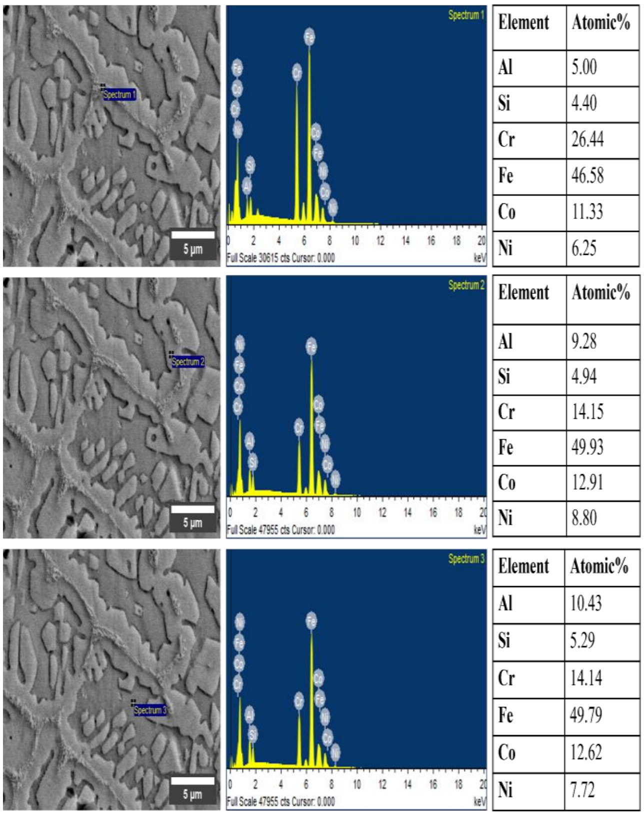

Element	Atomic%
Al	5.00
Si	4.40
Cr	26.44
Fe	46.58
Co	11.33
Ni	6.25

Element	Atomic%
Al	9.28
Si	4.94
Cr	14.15
Fe	49.93
Co	12.91
Ni	8.80

Element	Atomic%
Al	10.43
Si	5.29
Cr	14.14
Fe	49.79
Co	12.62
Ni	7.72

Fig. 5. EDS point scan graph of samples S-120A cladded zone.

The addition of Si atoms creates lattice distortion due to smaller radius [44], turned FCC structure to BCC due to BCC stabilizer in nature [45,46]. The development of various morphology is basically depending on temperature gradient caused by the heat input [25], from the solidification view the changes in dendritic morphology are related with the ratio of temperature gradient and solidification rate [35]. It was observed at higher heat input (247.13 J/mm) the grain boundary (GB) phases (bright region) become wider and more feathery structures compared to other heat inputs. These feathery dendritic structures extend in inter dendritic grain (ID), reduces ID, which is shown in microstructure as dark regions, this may be due to grain coarsening resulted in high heat input. On the other hand, compared to medium heat input (211.26 J/mm), the low heat input (174.41 J/mm) cladded sample illustrated wider ID and less GB. The different contrast of ID and GB x in regions due to variation in heat inputs.

EDS point scan at various phase regions of high heat input cladded sample (at cross section area) were shown in Figure 5 as a representation of other heat inputs, however, measured values of low and medium heat inputs are tabulated and mentioned in Table 6.

In case of high heat input, Cr, Fe and Co rich phase were identified in the segregated region formed on GB, in same region depletion of Al, Si and Ni were also seen as compared to GB and ID region, similar case was seen in other medium and low heat inputs as mentioned in Table 6. On the other hand, there is slightly variation of composition in ID and GB regions, in ID region higher atomic fraction of Al and Ni were observed whereas depletion of Co and Cr is identified as compared to GB.

Table 6. EDS of sample S-80A and S-100A

Atomic %	S-80A			S-100A		
Element	Region on GB Phase	GB Region	ID Region	Region on GB Phase	GB Region	ID region
Al	6.21	10.16	11.11	4.93	9.19	10.46
Si	4.81	5.75	5.17	5.59	5.16	5.45
Cr	25.31	13.27	13.23	26.24	14.13	13.98
Fe	44.21	49.12	49.11	45.93	49.71	49.68
Co	12.1	12.21	13.53	11.19	12.41	12.59
Ni	7.15	9.49	7.85	6.12	9.4	7.84

Increasing trend of Al indicated the transition of phase to FCC+BCC, similar reported by chengbin et al. [46], Si almost uniformly distributed not much significant variation were observed in both dendrites [40]. Al variation is more in ID then GB and very low segregation in region on GB. This may be due to intense mixing or high dilution effect. From the EDS scan it is believed that the ΔH_{mix} of Fe, Cr and Co elements are more negative, therefore it may slightly be enriched at the region on GB in all cases.

3.4 Microhardness Analysis

Figure 6(a) showed a diamond-shaped indentation resulting from the micro-hardness test, which is divided into two distinct regions: the HEA layer and the substrate, with a transition zone between them. Figure 6(b) illustrated the micro-hardness profile of the substrate and $AlCoCeFeNiSi_{0.3}$ HEA cladding of varying heat input, characterized by three main stages: HEA cladded layer, HAZ, and substrate.

It is observed that S-80A, S-100A and S-120 samples have average micro-hardness of 394.2 $HV_{0.3}$, 472.1 $HV_{0.3}$, and 517.6 $HV_{0.3}$ respectively, whereas substrate has hardness of 213.7 $HV_{0.3.}$ It is notable that S-120A has increased more than 2.4 times the hardness of the substrate. S-100A and S-80A have 2.2 times and 1.8 times respectively that of substrate hardness.

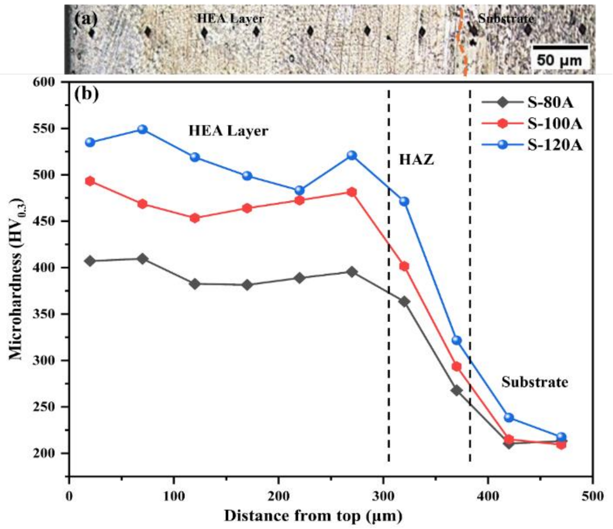

Fig. 6. Microhardness curve (a) Images of indentation, (b) Micro-hardness of substrate and HEA $AlCoCrFeNiSi_{0.3}$

Notably, the hardness value in the region between the coating and the substrate exhibits a progressive decline, influenced by the combined effects of the

metallurgical interface and the heat-affected zone. It is observed that the hardness increased with increasing heat input and measured highest in case of high heat input, this may be due to high dilution effect. It is believed that there may be a minor impact of columnar to refined equiaxed transition on micro-hardness. The presence of Si content has a smaller radius helped in severe distortion in BCC phase, also strengthening effect of solid solution influenced micro-hardness. The equiaxed grain exhibited the highest strength compared to columnar grain as heat input increased (247.13 J/mm), a larger number of equiaxed grains were observed compared to low heat input, which is also caused to increase the hardness in high heat input sample compared to others. High Fe and Cr content also caused to increase the hardness in high heat input due to intense mixing of elements and/or high dilution effect as confirmed in EDS scan.

3.4 Corrosion Analysis

Figure 7 showed the potentiodynamic polarization curves for the substrate and the $AlCoFeCrNiSi_{0.3}$ HEA cladding at varying heat input in a 3.5% NaCl solution, and the electrochemical parameters of the various cladded samples, including corrosion potential (E_{corr}), corrosion current density (I_{corr}), and pitting potential (E_{pit}) are summarized in Table 7.

The corrosion potential (E_{corr}) serves as a thermodynamic indicator of the material's susceptibility to corrosion, while the corrosion current density (I_{corr}) provides a kinetic measure of the corrosion rate [47].Additionally, the pitting potential (E_{pit}) assesses the materials resistance to pitting corrosion [48]. It is observed that passive region and stable region of the cladded layer have greater anodic polarization compared to substrate, higher I_{corr} is measured in substrate compared to all heat input in 3.5 % NaCl solution, which indicated that the $AlCoFeCrNiSi_{0.3}$ HEA alloy showed better corrosion resistance in NaCl solution compared to substrate.

It is known that the formation of passive film is key to retarded the corrosion process of metals, and alloying elements such as Al and Cr in HEAs have been reported to be able to form passive film in an NaCl environment [49]. The corrosion resistance could also be improved by the multiple elements preventing the formation of local anodic sites. The electrochemical reaction is basically anodic and cathodic reaction [50]. The behavior of HEA in NaCl is represented as follows [47,50].

Anodic process: $HEA \rightarrow HEA^{2+} + 2e^-$

Cathodic process: $2H + 2e^- \rightarrow H_2$

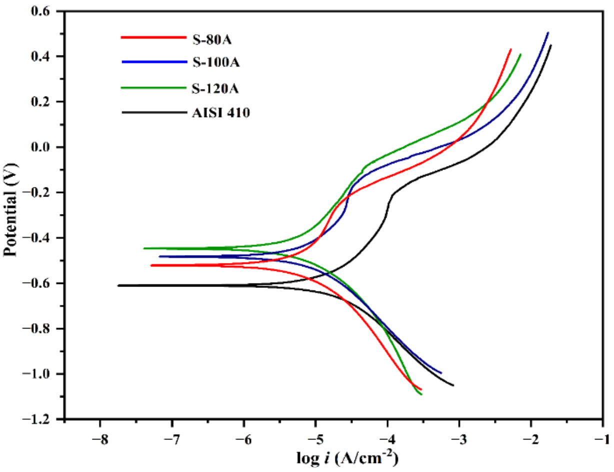

Fig. 7. Potentiodynamic polarization curve of HEA $AlCoCrFeNiSi_{0.3}$ and AISI 410 substrate

Table 7. Electrochemical parameters of HEA $AlCoCrFeNiSi_{0.3}$ and AISI 410 substrate in 3.5 % NaCl solution

Sample	E_{corr}(V)	I_{corr}(μA.cm^{-2})	E_{pit}(V)
S-80 A	-0.5241	5.098	-0.218
S-100 A	-0.4830	4.832	-0.162
S-120 A	-0.4505	3.848	-0.096
AISI 410	-0.6091	12.259	-0.251

Where HEA signifies metal atoms such as Al, Co, Cr, Fe, Ni and Si and so on. After test the corrosion product (after active and reactive dissolution) may be H_2 gas and metal cation (M^{2+}), due to the constant movement of metal ions dissolved from different phases in the solution, the metal ions adsorbed on the surfaces of FCC and BCC phases would be mixed [49,52]. For the $AlCoFeCrNiSi_{0.3}$ HEA, it is believed that Cr_2O_3 in the passive film may also played an important role in protecting corrosion [51].

The improved in corrosion resistance may also due to entropy alloy composition, addition of Si, promoted formation of the BCC phase, and reduction of grain size [52]. The addition of Si resulted in slight change in the passivation current density and passivation potential, which indicating the formation of protective passive film on the surface restricted the materials dissolution [27,50,53]. Among the cladded samples of different heat input assessment, it is noted that the higher heat input indicated lower I_{corr} and higher E_{corr} value compared to low heat input, this confirms that the lower heat input process resulted in a deterioration in the electrochemical corrosion resistance and led to a higher corrosion rate. However, from Table 7, the

S-100A sample showed better corrosion resistance than low heat input sample, but less resistance than high heat input sample.

4. CONCLUSION

$AlCoFeCrNiSi_{0.3}$ high entropy alloy (HEA) claddings were successfully applied on AISI 410 stainless steel using TIG cladding at varying heat inputs without any cracks or pores. XRD analysis revealed the presence of BCC and FCC solid solution phases. Microstructural studies showed a transition from columnar to equiaxed grains with increased heat input, and elemental segregation of Fe, Cr, and Co at grain boundaries. The highest micro-hardness (2.4 times of the substrate) was achieved in the high heat input sample (S-120A) attributed to refined grains and increased lattice strain. Corrosion tests in 3.5% NaCl solution showed all HEA samples showed better corrosion resistance than substrate. S-120A exhibiting the lowest corrosion rate due to Si addition and grain refinement. These improvements are attributed to solid solution strengthening, lattice distortion, and passive film formation. The study confirms TIG cladding as an effective and economical method to enhance hardness and corrosion resistance of AISI 410 for aggressive environments.

REFERENCES

[1] R V, Shanmugam NS, Kumar NP, Kumar KK, Kannan AR. Microstructure, mechanical properties, and corrosion behaviour of wire arc additive manufactured martensitic stainless steel 410 for pressure vessel applications. Int J Press Vessel Pip. 2024 Jun;209:105171. doi:10.1016/j.ijpvp.2024.105171.

[2] De Paula MA, Ribeiro MV, Souza JVC, Kondo MY. Analysis of the performance of coated carbide cutting tools in the machining of martensitic stainless steel AISI 410 in dry and MQL conditions. Mater Res Express. 2018 Oct;6(1):016512. doi:10.1088/2053-1591/aae28b.

[3] Saravanan G, et al. Assessment of wear properties on treated AISI 410 martensitic stainless steel by annealing process. E3S Web Conf. 2023;391:01108. doi:10.1051/e3sconf/202339101108.

[4] Zunko H, Turk C. Martensitic stainless steels for food contact applications. Berg Huettenmaenn Monatsh. 2022 Sep;167(9):408-415. doi:10.1007/s00501-022-01267-7.

[5] Kang HK, Lee H, Oh CS, Yoon J. Microstructure and mechanical properties of laser direct energy deposited martensitic stainless steel 410. Micromachines. 2024 Jun;15(7):837. doi:10.3390/mi15070837.

[6] Puli R, Kumar EN, Janaki Ram GD. Characterization of friction surfaced martensitic stainless steel (AISI 410) coatings. Trans Indian Inst Met. 2011 Feb;64(1-2):41-45. doi:10.1007/s12666-011-0008-6.

[7] Ren H, et al. High-performance AlCoCrFeNi high entropy alloy with marine application perspective. J Mater Res Technol. 2023 Jul;25:6751-6763. doi:10.1016/j.jmrt.2023.07.135.

[8] Huang M. Role of martensitic transformation sequences on deformation-induced martensitic transformation at high strain rates: A quasi in-situ study. Mater Sci. 2022.

[9] Singh G, Goyal K. Performance evaluation of hard faced turbine steel under slurry erosion conditions. J Mater Environ Sci. 2018;9(7):2109-2121.

[10] Aribo S, Barker R, Hu X, Neville A. Erosion–corrosion behaviour of lean duplex stainless steels in 3.5% NaCl solution. Wear. 2013 Apr;302(1-2):1602-1608. doi:10.1016/j.wear.2012.12.007.

[11] Toro A, Sinatora A, Tanaka DK, Tschiptschin AP. Corrosion–erosion of nitrogen bearing martensitic stainless steels in seawater–quartz slurry. Wear. 2001 Oct;251(1-12):1257-1264. doi:10.1016/S0043-1648(01)00765-7.

[12] Meijun L, Xu L, Zhu C, Li Z, Wei S. Research progress of high entropy alloy: Surface treatment improves friction and wear properties. J Mater Res Technol. 2024 Jan;28:752-773. doi:10.1016/j.jmrt.2023.12.011.

[13] Sharma A. High entropy alloy coatings and technology. Coatings. 2021 Mar;11(4):372. doi:10.3390/coatings11040372.

[14] El-Hadad S. High entropy alloys: The materials of future. Int J Mater Technol Innov. 2022 Apr;2(1):67-84. doi:10.21608/ijmti.2022.118565.1046.

[15] Tsai MH, Yeh JW. High-entropy alloys: A critical review. Mater Res Lett. 2014 Jul;2(3):107-123. doi:10.1080/21663831.2014.912690.

[16] Chen J, et al. A review on fundamental of high entropy alloys with promising high–temperature properties. J Alloys Compd. 2018 Sep;760:15-30. doi:10.1016/j.jallcom.2018.05.067.

[17] Cui K, Zhang Y. High-entropy alloy films. Coatings. 2023 Mar;13(3):635. doi:10.3390/coatings13030635.

[18] Kumar S. Comprehensive review on high entropy alloy-based coating. Surf Coat Technol. 2024 Feb;477:130327. doi:10.1016/j.surfcoat.2023.130327.

[19] Yang YF, et al. High entropy alloys: A review of preparation techniques, properties and industry applications. J Alloys Compd. 2025 Jan;1010:177691. doi:10.1016/j.jallcom.2024.177691.

[20] Alam MS. Recent trends in surface cladding on AISI 1045 steel substrate: A review. In: Functional Materials and Applied Physics. 2022 Apr. p. 94-101. doi:10.21741/9781644901878-13.

[21] Wang Z. Application of automatic TIG welding for Yamal LNG process piping fabrication. OGCE. 2018;6(4):44. doi:10.11648/j.ogce.20180604.11.

[22] Oliveira JP, Barbosa D, Fernandes FMB, Miranda RM. Tungsten inert gas (TIG) welding of Ni-rich NiTi plates: functional behavior. Smart Mater Struct. 2016 Mar;25(3):03LT01. doi:10.1088/0964-1726/25/3/03LT01.

[23] Mutașcu D, Karancsi O, Mitelea I, Crăciunescu CM, Buzdugan D, Uțu ID. Pulsed TIG cladding of a highly carbon-, chromium-, molybdenum-, niobium-, tungsten- and vanadium-alloyed flux-cored wire electrode on duplex stainless steel X2CrNiMoN 22-5-3. Materials. 2023 Jun;16(13):4557. doi:10.3390/ma16134557.

[24] Huo W, Shi H, Ren X, Zhang J. Microstructure and wear behavior of CoCrFeMnNbNi high-entropy alloy coating by TIG cladding. Adv Mater Sci Eng. 2015;2015:1-5. doi:10.1155/2015/647351.

[25] Fan Q, et al. AlCoCrFeNi high-entropy alloy coatings prepared by gas tungsten arc cladding: Microstructure, mechanical and corrosion properties. Intermetallics. 2021 Nov;138:107337. doi:10.1016/j.intermet.2021.107337.

[26] He Y, Cong M, Lei W, Ding Y, Xv T, Han Z. Microstructure, mechanical and corrosion properties of FeCrNiCoMnSi0.1 high-entropy alloy coating via TIG arc melting technology and high-frequency ultrasonic impact with welding. Mater Today Adv. 2023 Dec;20:100443. doi:10.1016/j.mtadv.2023.100443.

[27] Liu H, Sun S, Zhang T, Zhang G, Yang H, Hao J. Effect of Si addition on microstructure and wear behavior of AlCoCrFeNi high-entropy alloy coatings prepared by laser cladding. Surf Coat Technol. 2021 Jan;405:126522. doi:10.1016/j.surfcoat.2020.126522.

[28] Liu H, Zhang T, Sun S, Zhang G, Tian X, Chen P. Microstructure and dislocation density of AlCoCrFeNiSix high entropy alloy coatings by laser cladding. Mater Lett. 2021 Jan;283:128746. doi:10.1016/j.matlet.2020.128746.

[29] Chandel DK, Thakur L, Kumar V. An investigation on the tribological behaviour of AlCrCuNiFe high entropy alloy optimized TIG weld cladding in room temperature conditions. Tribol Int. 2023 Nov;189:108982. doi:10.1016/j.triboint.2023.108982.

[30] Kumar Chandel D, Thakur L, Kumar V. Investigation of the failure behaviour of equiatomic AlCrCuNiFe based high entropy alloy TIG weld cladding. Eng Fail Anal. 2024 Nov;165:108836. doi:10.1016/j.engfailanal.2024.108836.

[31] Girisha KG, Sreenivas Rao KV. Improvement of corrosion resistance of AISI 410 martensitic steel using plasma coating. Mater Today Proc. 2018;5(2):7622-7627. doi:10.1016/j.matpr.2017.11.436.

[32] Puli R, Janaki Ram GD. Wear and corrosion performance of AISI 410 martensitic stainless steel coatings produced using friction surfacing and manual metal arc welding. Surf Coat Technol. 2012 Sep;209:1-7. doi:10.1016/j.surfcoat.2012.06.075.

[33] Chen Z, et al. Study on microstructure and properties of AlCoCrFeNi high-entropy alloys by extreme high-speed laser cladding. Coatings. 2024 Nov;14(11):1394. doi:10.3390/coatings14111394.

[34] Tabish TA, Abbas T, Farhan M, Atiq S, Butt TZ. Effect of heat input on microstructure and mechanical properties of the TIG welded joints of AISI 304 stainless steel. 2014.

[35] Yu P, Kou S, Lin CM. Solidification and liquation cracking in welds of high entropy CoCrFeNiCux alloys. Materials. 2023 Aug;16(16):5621. doi:10.3390/ma16165621.

[36] Zhang Y, et al. Microstructures and properties of high-entropy alloys. Prog Mater Sci. 2014 Apr;61:1-93. doi:10.1016/j.pmatsci.2013.10.001.

[37] Zhang S, et al. Microstructure and high temperature erosion behavior of laser cladded CoCrFeNiSi high entropy alloy coating. Surf Coat Technol. 2021 Jul;417:127218. doi:10.1016/j.surfcoat.2021.127218.

[38] Hao X, et al. Friction–wear behaviors and microstructure of AlTiVCrNb lightweight refractory high-entropy alloy coating prepared by laser cladding on Ti–6Al–4V substrate. J Mater Res Technol. 2024 Mar;29:1-11. doi:10.1016/j.jmrt.2024.01.107.

[39] Liu WH, Wu Y, He JY, Zhang Y, Liu CT, Lu ZP. The phase competition and stability of high-entropy

alloys. JOM. 2014 Oct;66(10):1973-1983. doi:10.1007/s11837-014-1119-4.

[40] B V, A X M. Development of high entropy alloys (HEAs): Current trends. Heliyon. 2024 Apr;10(7):e26464. doi:10.1016/j.heliyon.2024.e26464.

[41] Chen Q, Zhou K, Jiang L, Lu Y, Li T. Effects of Fe content on microstructures and properties of AlCoCrFexNi high-entropy alloys. Arab J Sci Eng. 2015 Dec;40(12):3657-3663. doi:10.1007/s13369-015-1784-9.

[42] Zhang G, Liu H, Tian X, Chen P, Yang H, Hao J. Microstructure and properties of AlCoCrFeNiSi high-entropy alloy coating on AISI 304 stainless steel by laser cladding. J Mater Eng Perform. 2020 Jan;29(1):278-288. doi:10.1007/s11665-020-04586-3.

[43] Xiang CH, Zhang ZM, Fu HM, Han EH, Zhang HF, Wang JQ. Microstructure and corrosion behavior of AlCoCrFeNiSi0.1 high-entropy alloy. Intermetallics. 2019;114:106599.

[44] Zhang Y, Ren L, Shen G, Zhu L, Zhang J. Microstructure and mechanical properties of AISI 410S ferritic stainless steel narrow gap weld using flux strip constraining arc welding. Mater Charact. 2023;206:113380.

[45] Cheng P, Zhao Y, Xu X, Wang S, Sun Y, Hou H. Microstructural evolution and mechanical properties of Al0.3CoCrFeNiSix high-entropy alloys containing coherent nanometer-scaled precipitates. Mater Sci Eng A. 2020;772:138681.

[46] Kadoi K, Ueno S, Inoue H. Effects of ferrite content and concentrations of carbon and silicon on weld solidification cracking susceptibility of stainless steels. J Mater Res Technol. 2023;25:1314-1321.

[47] Wei C, Li L, Lu Y, Du X, Wang T. Evolution of microstructure and mechanical properties of as-cast AlxCrFe2Ni2 high-entropy alloys with Al content. Metall Mater Trans A. 2021 May;52(5):1850-1860. doi:10.1007/s11661-021-06195-8.

[48] Wei S, Su H. Mechanistic aspects of factors affecting pitting corrosion of metallic materials for marine application: A review paper. Int J Electrochem Sci. 2019 Apr;14(4):3949-3967. doi:10.20964/2019.04.02.

[49] Guo Y, et al. Pitting corrosion mechanism of BCC+FCC dual-phase structured laser cladding FeCoCrNiAl0.5Ti0.5 HEAs coating. J Alloys Compd. 2024 Apr;980:173643. doi:10.1016/j.jallcom.2024.173643.

[50] Yang H, et al. Effect of silicon addition on the corrosion resistance of Al0.2CoCrFe1.5Ni high-entropy alloy in saline solution. J Alloys Compd. 2023 Nov;964:171226. doi:10.1016/j.jallcom.2023.171226.

[51] Huang PC, Chu PC, Wang JZ, Lin WC. Investigation of the corrosion behavior of AlCoCrFeNi high-entropy alloy in 0.5 M sulfuric acid solution using hard and soft X-ray photoelectron spectroscopy.

[52] Yen CC, et al. Corrosion mechanism of annealed equiatomic AlCoCrFeNi tri-phase high-entropy alloy in 0.5 M H2SO4 aerated aqueous solution. Corros Sci. 2019 Aug;157:462-471. doi:10.1016/j.corsci.2019.06.024.

[53] Chang Y, et al. Effect of Si on the corrosion resistance of AlZrNbTi lightweight refractory high-entropy alloys in acidic environment.